WS_2/MoS_2 heterostructures via thermal treatment of MoS_2 layers electrostatically functionalized with W_3S_4 molecular clusters

Marc Morant-Giner,[a] Isaac Brotons-Alcazar,[a] Nikita Y. Shmelev,[b] Artem L. Gushchin,[b] Luke Norman,[c] Andrei N. Khlobystov,[c] Antonio Alberola,[a] Sergio Tatay,[a] J. Canet-Ferrer,[a] Alicia Forment-Aliaga,[a] and Eugenio Coronado*[a]*

[a] M. Morant-Giner, I. Brotons, A. Dr. Alberola, Dr. S. Tatay, Dr. J. Canet-Ferrer, Dr. A. Forment-Aliaga and Prof. E. Coronado

Instituto de Ciencia Molecular

Universitat de València

C/ Catedrático José Beltrán, 2; 46980 Paterna, Spain

E-mail: alicia.forment@uv.es; eugenio.coronado@uv.es

[b] N. Y. Shmelev and Dr. A. L. Gushchin

Nikolaev Institute of Inorganic Chemistry

Siberian Branch of Russian Academy of Sciences

3, Acad. Lavrentiev Ave.; Novosibirsk, 630090, Russia

Novosibirsk State University

1 Pirogov str.; Novosibirsk, 630090, Russia

[c] L. Norman and Prof. A. N. Khlobystov

School of Chemistry

University of Nottingham

University Park.; Nottingham, NG7 2RD, UK

Abstract: The preparation of 2D stacked layers that combine flakes of different nature, gives rise to countless number of heterostructures where new band alignments, defined at the interfaces, control the electronic properties of the system. Among the large family of 2D/2D heterostructures, the one formed by the combination of the most common semiconducting transition metal dichalcogenides WS_2/MoS_2, has awaken great interest due to its photovoltaic and photoelectrochemical properties. Solution as well as dry physical methods have been developed to optimize the synthesis of these heterostructures. Here a suspension of negatively charged MoS_2 flakes is mixed with a methanolic solution of a cationic W_3S_4-core cluster, giving rise to a homogeneous distribution of the clusters over the layers. In a second step, a calcination under N_2 of this molecular/2D heterostructure leads to the formation of clean WS_2/MoS_2 heterostructures where the photoluminescence of both counterparts is quenched, proving an efficient interlayer coupling. Thus, this chemical method combines the advantages of a solution approach (simple, scalable and low-cost) with the good quality interfaces reached by using more complicated traditional physical methods.

Introduction

Since the isolation of graphene, two-dimensional (2D) materials have become a hot focus of interest in materials science because of their strong 2D quantum confinement and large high surface-area-to-volume ratios.[1] Nowadays, in addition to downsizing layered materials to the 2D limit, the scientific community endeavours to study and harness the novel properties and synergistic effects arising from the combination of different 2D components into advanced functional heterostructures, especially in (bio)sensing,[2] electronics,[3] optoelectronics,[3] and (photo)catalysis.[4]

Among the most studied 2D materials, the large family of transition metal dichalcogenides (TMDCs) stands out due to its wide variety of electronic properties, ranging from semiconductors[5] to superconductors.[6] TMDCs are layered compounds consisting of vertically stacked X-M-X slabs, with a general chemical formula of MX_2, where M stands for a transition metal (usually pertaining to groups IV-VII) and X refers to a chalcogen (S, Se, or Te).[7,8] As the interlayer van der Waals (vdW) interactions are much weaker than the intralayer covalent bonding, 2D X-M-X slabs can be readily produced by exfoliation.[9] In relation to their structure, the most common polytypes are 1T and 2H (or 1H in the case of monolayer), where the digit alludes to the number of X-Mo-X layers per unit cell and the letter indicates the structural symmetry (*e.g.*, T = tetragonal and H = hexagonal).[10]

Interestingly, 2D semiconducting TMDCs display a broad spectrum of possibilities in photoelectrocatalysis, particularly in the branch concerning energy storage and conversion.[11] Currently, titanic efforts are addressed to speed up the rate of hydrogen and oxygen evolution reactions (HER and OER, respectively) occurring during the well-known photoelectrochemical (PEC) water splitting process, where TMDCs can play a crucial role.

Amongst semiconducting TMDCs, isostructural WS_2 and MoS_2 in their thermodynamically stable 2H phase are robust under wet conditions, including acidic media,[12] and exhibit exceptional light-matter interactions, like photovoltaic properties.[13,14] Apart from possessing a hydrogen binding energy close to that of Pt-group,[15] computational studies appear to indicate that the valence band

edges of WS_2 and MoS_2 monolayers straddle the water oxidation potential.[16,17] Interestingly, in WS_2/MoS_2 heterostructures, the energy band alignment existing at the interface of both materials not only promotes the electron hole dissociation but also extends the charge carrier lifetime, enhancing the diffusion length, which renders this kind of heterojunction appealing for optoelectronic and light harvesting applications.[18,19]

As an example of the relevance of these heterostructures, high-quality large-area WS_2/MoS_2 heterojunctions synthesized by chemical vapour deposition (CVD) have evidenced a noteworthy photocatalytic performance for salt-water oxidation.[20] However, also WS_2/MoS_2 heterostructures prepared by a straightforward and low-cost liquid-phase method can oxidize water in acidic environment (without the need of using cocatalysts and protective layers), while increasing the incident-photon-to-current-efficiency by a factor of 10, in comparison to individual constituents.[21] Also in photoanodes based on WS_2/MoS_2 heterostructures prepared by wet methods, photocurrent density of the WS_2/MoS_2 sample turned out to be 8 and 4 times higher than those reported for pure WS_2 and MoS_2, respectively. This enhancement suggests an efficient charge separation inside the photoanode as well as a low interface resistance of the electrode-electrolyte.[22]

The different strategies addressed to prepare WS_2/MoS_2 and other 2D/2D heterostructures can be classified in two main groups: (i) solid-state approaches, and (ii) wet methods. The former refers to the stacking of flakes obtained through dry mechanical exfoliation methods (deterministic transfer). Albeit this approach ensures the high quality of the stacked layers, it suffers from several issues: active implication by the operator, difficulty to scale-up the process, possibility of enclosing contamination between layers, lack of control when stacking the 2D components, and relatively weak interlayer coupling. Nevertheless, solid-state methods also refer to the sequential or simultaneous growth of both 2D components via CVD or physical vapour deposition (PVD), overcoming the scalability problem to some extent and often creating perfect heterojunctions (epitaxial growth) in virtue of the isostructural nature of the components (*e.g.*, WS_2 and MoS_2). However, high temperature and vacuum conditions contribute to increase the complexity of this process. Alternatively, a simple and scalable option is the use of wet methods, like the electrostatic wet-chemical assembling of charged ultrathin layers[23] by means of layer by layer,[24] flocculation,[25,26] or Langmuir-Blodgett techniques.[27] Nevertheless, these approaches have to face the uncontrolled organization of the flakes inside each slab of the final multilayer system and the fact that different species in solution can be occluded between the 2D components, hindering a good interaction between them.

Within the wet strategies, those involving chemical reactions are peaking in popularity. Thus, 2D/2D heterostructures can also be prepared *via* hydrothermal growth of one 2D material on top of the other or by decoration of one 2D component with a molecular system prone to undergo thermal decomposition into another 2D material. Some examples of this strategy are the hydrothermal growth of MoS_2 layers on WS_2 flakes[28] and the fabrication of WS_2 flakes on graphene by dry calcination. The latter represents a unique way to guarantee the removal of residual organic molecules from the heterostructure,[29,30] a clear advantage in the face of hydrothermal approach.

Inspired by these methods, we report here a new two-step strategy to form WS_2/MoS_2 heterojunctions (Scheme 1), which involves first the electrostatic functionalization of chemically exfoliated MoS_2 (ce-MoS_2) layers with a tungsten cluster in methanol:water solution (herein referred as cluster@MoS_2) and second, a dry thermal treatment of this composite to form WS_2 flakes on the MoS_2 layers.

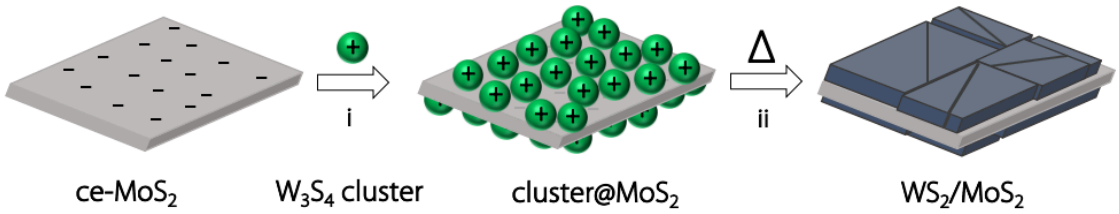

Scheme 1. *Pictorial representation of WS_2/MoS_2 synthesis: (i) Synthesis of cluster@MoS_2; (ii) Calcination of cluster@MoS_2 to give rise to the final WS_2/MoS_2 heterostructure.*

The proposed method relies on the homogeneous distribution of the cluster over ce-MoS_2 layers thanks to the electrostatic interactions established between the cationic cluster and the anionic layers, which hinders cluster aggregations.

Results and Discussion

To prepare the WS_2/MoS_2 heterostructures, we used $[W_3S_4(tu)_8(H_2O)]Cl_4{\cdot}2H_2O$ cluster (in short W_3S_4 cluster) as molecular source of WS_2 and ultrathin MoS_2 flakes (1-5 nm thick and 0.2-1.2 µm wide) produced by chemical exfoliation with *n*-BuLi[31] as underlying substrate. Even though the synthesis and thermal decomposition of $[W_3S_4(tu)_8(H_2O)]Cl_4{\cdot}2H_2O$ into WS_2 layers was reported in 2016,[32] the study on the morphology of the decomposition product has remained elusive until now. Thus, with the aim of completing the characterization process initiated by A. L. Gushchin and co-workers four years ago, high-resolution transmission electron microscopy (HR-TEM) images, along with X-ray photoelectron (XPS) and Raman spectra, are provided hereafter.

The calcination of the aforementioned W_3S_4 cluster in the 25-700 ºC range afforded ultrathin layers of WS_2. To minimize the oxidation of the ultrathin layers, the calcined material was preserved from the air exposure inside the thermogravimetric analysis (TGA) apparatus until it was completely cooled down to room temperature. If the W_3S_4 cluster is not well isolated from air, tungsten oxides can be formed.[30] Interestingly, equivalent Mo_3S_4 clusters can be synthetized and used as thermal precursors of MoS_2 layers.[33,34]

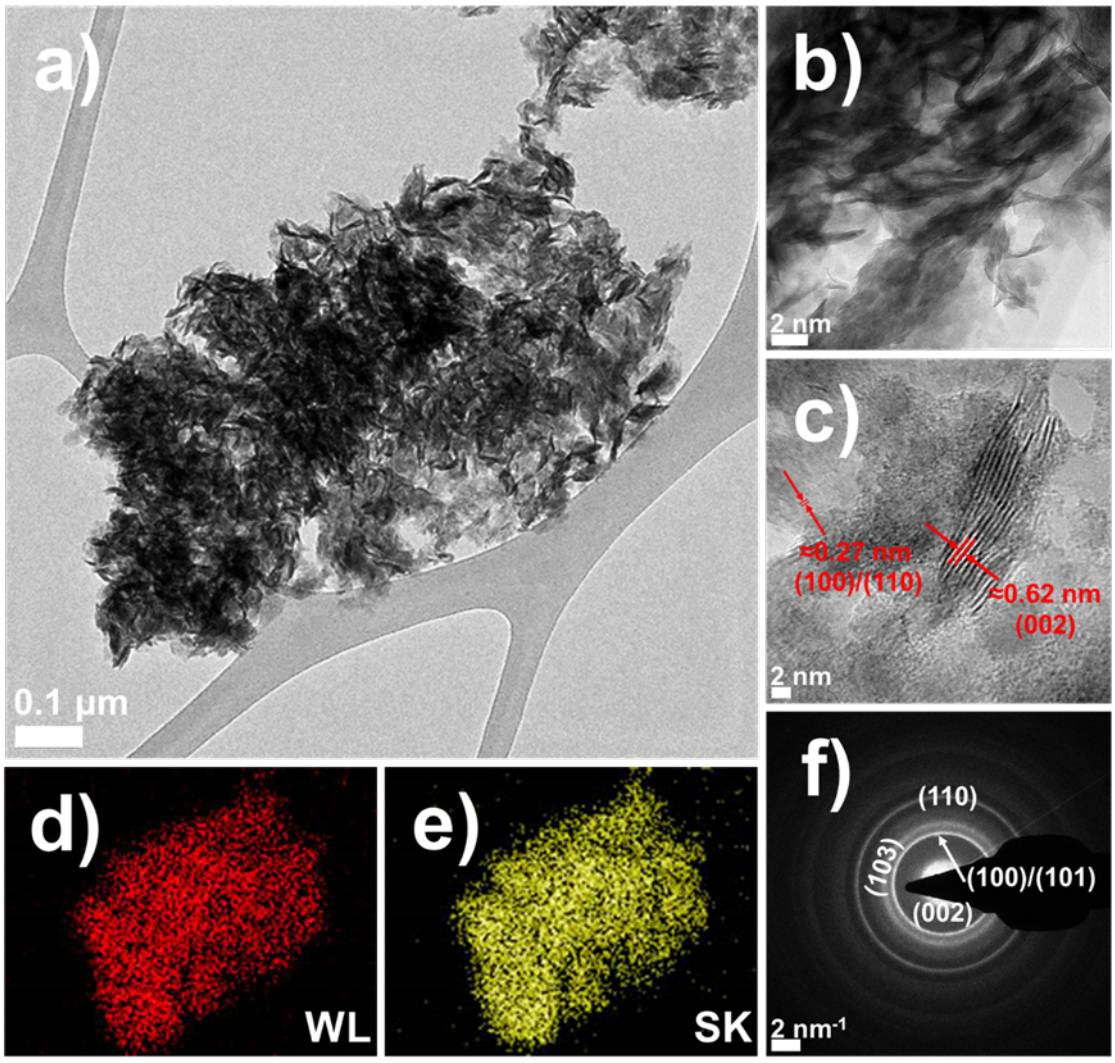

Figure 1. *a) TEM image of the material obtained by calcination of the W_3S_4 clusters; b) Zoomed TEM image showing the lamellar nature of the material; c) HR-TEM images showing different interplanar spacing values; d-e) EDS elemental mapping of the sample shown in (a); f) SAED pattern of the sample shown in (a).*

The morphology of the calcined material was analysed by HR-TEM. According to TEM images (**Figures 1a** and **1b**), this material has a lamellar structure. In the HR-TEM image (**Figure 1c**), fringes with interplanar spacing values of ≈0.27 and 0.61 nm are observed. These values are assignable to (100)/(101) and (002) planes of WS_2, respectively.[35] The energy-dispersive X-ray spectroscopy (EDS) elemental mapping (**Figures 1d** and **1e**) highlights a good matching between W and S signals, as expected for WS_2 flakes. From inside to outside, the SAED rings correspond to (002), (100)/(101), (103), and (110) planes of WS_2, respectively (**Figure 1f**). Moreover, the appearance of rings corroborates the polycrystalline nature of WS_2.

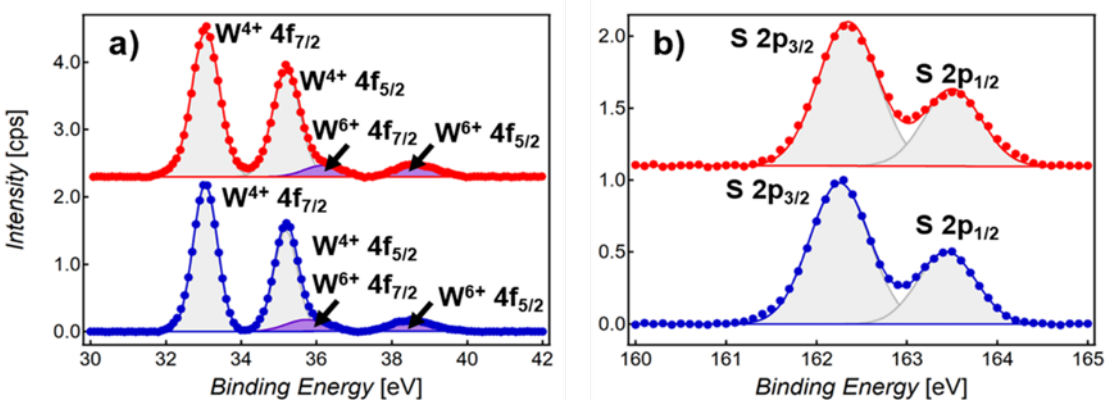

Figure 2. *a) W 4f XPS spectra of commercial WS_2 (blue) and calcined material (red) normalized using the S $2p_{3/2}$ signal; b) Normalized S 2p XPS spectra of commercial WS_2 (blue) and calcined material (red).*

The study of the composition of calcined material was conducted by XPS. W 4f spectrum (**Figure 2a**) is dominated by two intense peaks centred at ≈33.1 and 35.2 eV, which are related to 2H W^{4+} $4f_{7/2}$ and 2H W^{4+} $4f_{5/2}$ components, respectively.[36] As expected, WS_2 layers obtained by thermal decomposition only contains the thermodynamically stable 2H phase. Minor contributions observed at ≈36.2 and 38.7 eV arises from W^{6+} $4f_{7/2}$, and W^{6+} $4f_{5/2}$ components, respectively, indicating certain degree of oxidation (≈12.0% of WO_3 from total W).[35] Curiously, the commercial 2H-WS_2 used as reference contains approximately the same oxide percentage. The explanation to this fact could be that WS_2 edges are spontaneously oxidized to certain extent if manipulated in ambient conditions.[37] S 2p spectrum (**Figure 2b**) displays two well-defined peaks at ≈162.3 and 163.5 eV, which correspond to S^{2-} $2p_{3/2}$ and $2p_{1/2}$ components, respectively. Thus, all these values are in good agreement with those measured for commercial WS_2. The S:W molar ratio of the calcined material was estimated at 2.15.

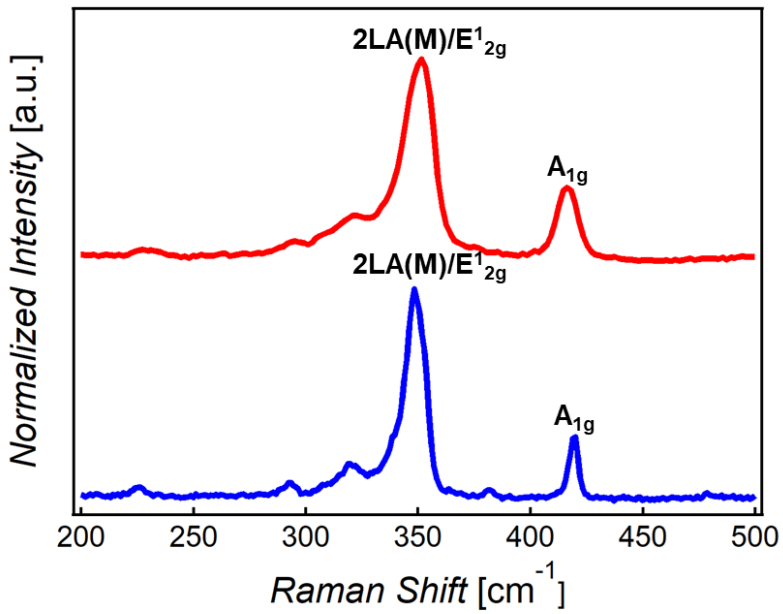

***Figure 3**. Normalized Raman spectra of commercial WS_2 (blue) and calcined material (red) at 532 nm excitation wavelength.*

The definitive proof that the calcined material corresponds to WS_2 layers was obtained from Raman spectroscopy. The most intense 2LA(M)/E^1_{2g} and A_{1g} peaks appear at ≈352 and 416 cm^{-1}, respectively (see **Figure 3**). Whilst 2LA(M) represents the longitudinal acoustic phonon at the M-point of the Brillouin zone (periodic compressions and expansions of the lattice that occur along the propagation direction),[38] the in-plane E^1_{2g} mode is related to the opposite vibration of two S atoms respect to the W atom between them and the out-of-plane A_{1g} mode describes the transverse vibration of S atoms in opposite directions.[39] The peak separation between 2LA/E^1_{2g} and A_{1g} modes (≈64 cm^{-1}) is consistent with at most 2H-WS_2 bi- or tri-layer entities integrated into a turbostratic stacking.[40] Overall, these results confirm the WS_2 nature of the calcined material.

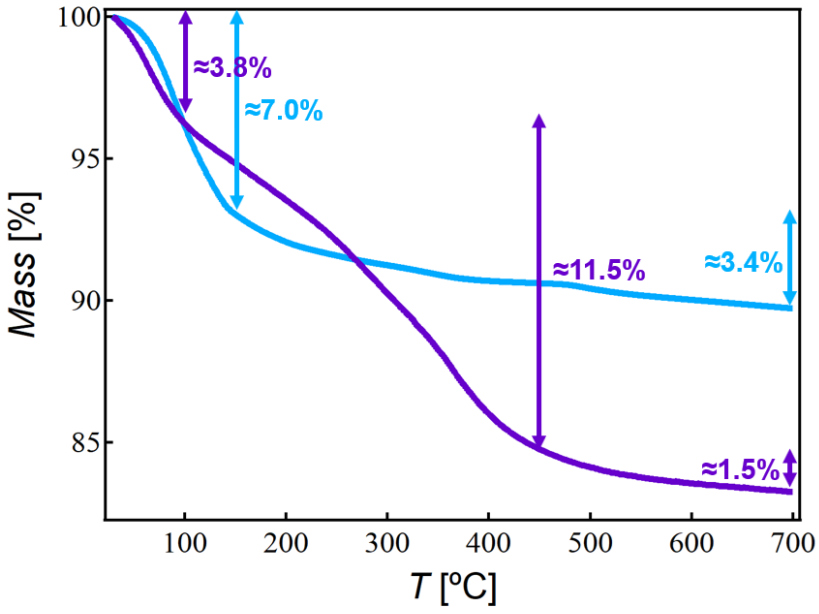

***Figure 4.** TGA plots of ce-MoS_2 flakes (bright blue) and cluster@MoS_2 composite (purple).*

Prior to the synthesis of WS_2/MoS_2 heterostructure, the thermal stability of ce-MoS_2 flakes under the conditions used to decompose the W_3S_4 clusters was evaluated. Thus, ce-MoS_2 flakes were calcined under inert atmosphere in the 25–700 °C range. In the TGA plot of ce-MoS_2 flakes (**Figure 4**), a significant mass drop of ≈7.0% in the 25-150 ºC accompanied by a steady and scant mass loss of ≈3.4% in the 150-700 ºC range were observed. Whilst the first drop corresponds to the removal of physisorbed water, the second one is due to the loss of S pertaining to MoS_2, since, as demonstrated in previous works, harsh intercalation conditions can affect the structural integrity of this compound.[41]

To synthesize cluster@MoS_2 (Scheme 1), a freshly prepared suspension of ce-MoS_2 flakes in water was mixed with a methanolic $[W_3S_4(tu)_8(H_2O)]Cl_4 \cdot 2H_2O$ solution, in a molar proportion of 1:5, respectively, under argon atmosphere. The mixture was allowed to react for 1 h under magnetic stirring and, after that, centrifuged. Whilst the supernatant was discarded, the remaining sediment was washed by a couple of redispersion/centrifugation cycles (with the goal of removing the unattached W_3S_4 cluster) and then vacuum-dried. At this point, it is important to remark that, owing to its high lability toward ligand substitution, some coordinated tu ligands can be replaced by water and/or methanol molecules during the reaction and washing process, changing the original composition of the W_3S_4 cluster.

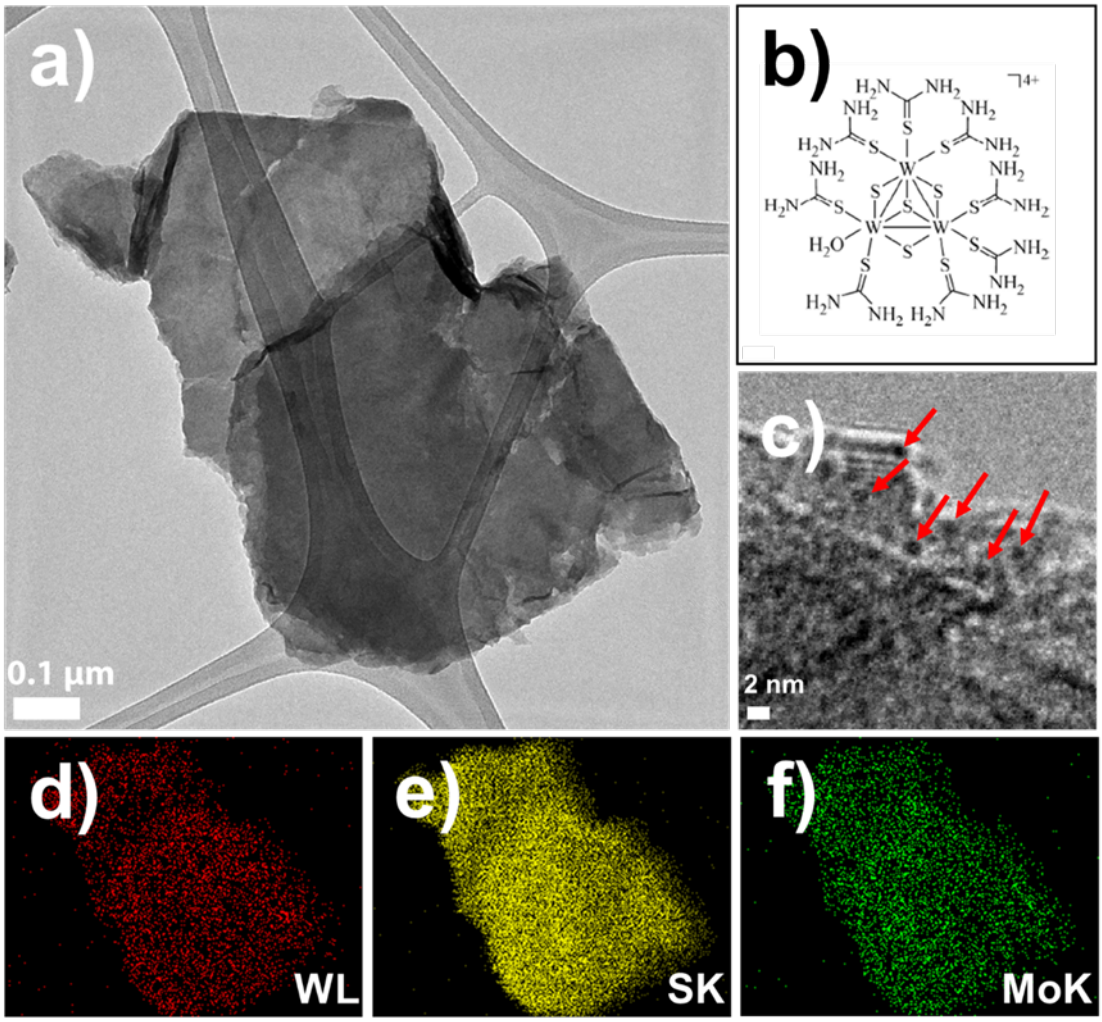

Figure 5. *a) TEM image of cluster@MoS_2 ; b) sketch of $[W_3S_4(tu)_8(H_2O)]^{4+}$ cluster; c) HR-TEM images of cluster@MoS_2. Red arrows point to clusters over MoS_2 surface; d-f) EDS elemental mapping of cluster@MoS_2 shown in (a).*

The morphology of cluster@MoS_2 was scanned by HR-TEM. According to TEM images (**Figure 5a**), ce-MoS_2 flakes show no morphological changes. The HR-TEM image (**Figures 5b** and **5c**) reveals black features over unmodified MoS_2 surface. In bright-field TEM, contrast is proportional to the square root of the atomic number of the element at issue. This is the reason why W_3S_4 clusters are imaged as black spots on thin MoS_2 flakes. Moreover, the EDS elemental mapping (**Figures 5d** and **5f**) evinces a homogeneous coverage of ce-MoS_2 flakes with trimetallic clusters.

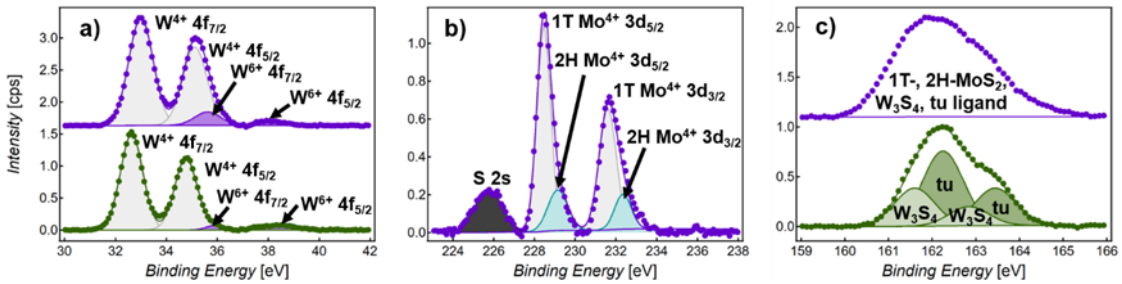

Figure 6. *a) W 4f XPS spectra of $[W_3S_4(tu)_8(H_2O)]Cl_4{\cdot}2H_2O$ (dark green) and cluster@MoS_2 (purple) normalized by using the S $2p_{3/2}$ signal; b) Mo 3d spectrum of cluster@MoS_2 normalized by using the S $2p_{3/2}$ signal; c) Normalized S 2p spectra of $[W_3S_4(tu)_8(H_2O)]Cl_4{\cdot}2H_2O$ (dark green) and cluster@MoS_2 (purple).*

To get useful information about the chemical composition, cluster@MoS_2 was analysed by XPS. W 4f spectrum (**Figure 6a bottom**) is dominated by two intense peaks centered at ≈33.0 and 35.1 eV, which are assigned to W^{4+} $4f_{7/2}$ and W^{4+} $4f_{5/2}$ components, respectively.[36] Minor contributions observed at ≈35.6 and 38.1 eV stem from W^{6+} $4f_{7/2}$, and W^{6+} $4f_{5/2}$ components, respectively, indicating certain degree of oxidation (≈9.1% of WO_3 from total W).[36] In this case, W^{4+} peaks are slightly shifted to high values respect to those of bare W_3S_4 cluster (32.6 and 34.7 eV, **Figure 6a top**). Most probably, this change indicates that some tu molecules have been replaced by water and/or methanol, without affecting the pristine oxidation state of W. Mo 3d spectrum (**Figure 6b**) shows five peaks located at ≈225.7, 228.5, 229.2, 231.6, and 232.3 eV, which correspond to S^{2-} 2s, 1T Mo^{4+} $3d_{5/2}$, 2H Mo^{4+} $3d_{5/2}$, 1T Mo^{4+} $3d_{3/2}$, and 1T Mo^{4+} $3d_{3/2}$ components, respectively.[42] 1T-MoS_2 (78.1%) dominates over 2H-MoS_2 (21.9%), as expected for ce-MoS_2 flakes prepared by using an excess of *n*-BuLi.[41] Thus, no phase transition is induced due to the attachment of the W_3S_4 cluster to the flakes, supporting the idea that there are only weak electrostatic interactions between both components. S 2p spectrum, located in the 159-166 eV range, (**Figure 6c**) includes signals arising from several chemical environments (1T-MoS_2, 2H-MoS_2, W_3S_4 core, and tu ligands), encumbering the deconvolution of S spectral region. According to the atomic percentage (At%) data, there is a S loss of ≈4.75%, which would confirm the lability of tu ligands. W:Mo molar ratio was determined as 1.61. Moreover, the XPS survey reveals the presence of Cl, suggesting that the positive charge of W_3S_4 cluster is not completely compensated by the excess of negative charge accumulated onto MoS_2 surface.

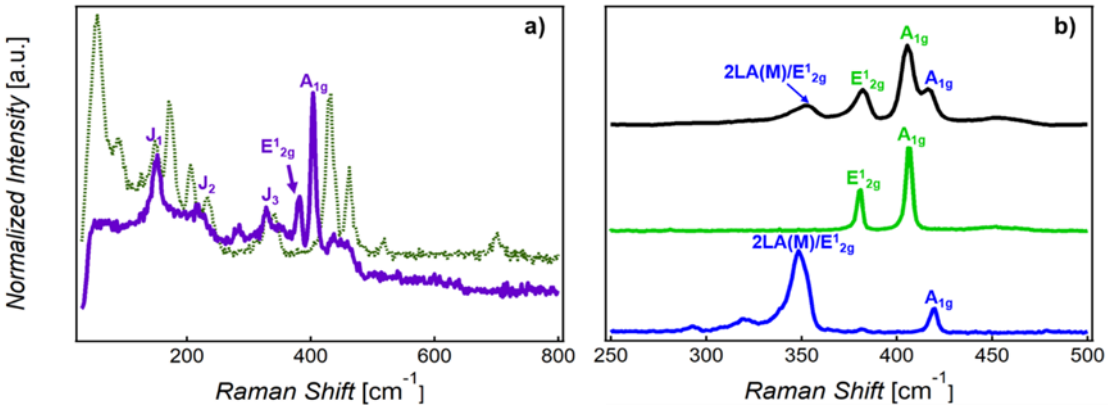

Figure 7. *Normalized Raman spectra at 532 nm excitation wavelength of a) $[W_3S_4(tu)_8(H_2O)]Cl_4{\cdot}2H_2O$ (dark green) and cluster@MoS_2 (purple) and b) commercial WS_2 (blue), commercial MoS_2 (bright green) and WS_2/MoS_2 (black).*

Cluster@MoS_2 was analysed by Raman spectroscopy. The resultant Raman spectrum (**Figure 7a**) uniquely shows MoS_2 peaks. The presence of the so-called J peaks at ≈152 (J_1), 220 (J_2), and 328 (J_3) cm^{-1}, characteristic of the superlattice structure of 1T-MoS_2,[43,44] reflects the abundance of this polytype in ce-MoS_2 flakes. J peaks arise from longitudinal acoustic phonon modes of 1T phase.[45] Because of the lower signal expected for the W_3S_4 cluster at the working excitation wavelength and the uniform distribution of this compound over MoS_2, no clear signatures of the W_3S_4 cluster were observed.

Finally, to obtain WS_2/MoS_2 heterostructures, cluster@MoS_2 was calcined in the 25–700 °C range, under inert atmosphere. To minimize the oxidation of the ultrathin layers, the resultant calcined material was preserved from the air exposure inside the TGA apparatus until it was completely cooled down to room temperature. If these precautions are not taken, MoO_2 nanowires can be formed during the calcination process (**Figure S1**).[46] In contrast to what happens for ce-MoS_2 flakes, the TGA resulting from composite calcination (**Figure 4**) shows two remarkable mass drops (≈3.8% in the 25-100 ºC range and ≈11.5% in the 100-450 ºC) followed by a steady mass loss (≈1.5% in the 450-700 ºC range). Whilst the first one would be associated with the removal of both methanol and water molecules, either physorbed or forming part of the W_3S_4 cluster, the second one would correspond to the dissociation of the remaining tu ligands. Additionally, it also cannot be ruled out the formation of volatile tungsten species, such as $WO_2(OH)_2$[47] and WCl_6. The final steady mass probably arises from a little loss of the S belonging to MoS_2 flakes.

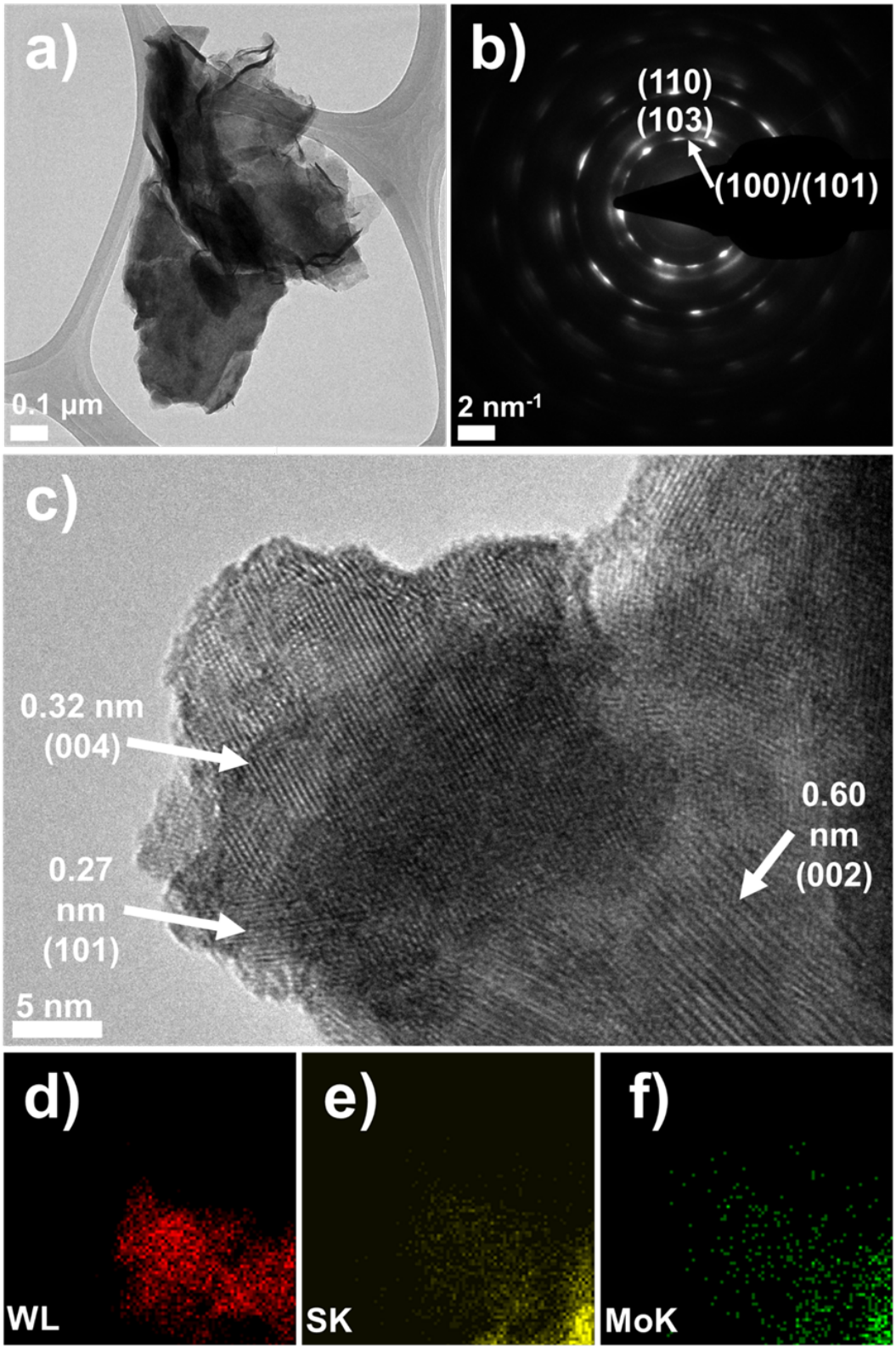

Figure 8. *a) TEM image of WS_2/MoS_2; b) SAED pattern of the sample shown in (a); c) HR-TEM image of WS_2/MoS_2 showing high crystalline WS_2 nanodomains; d-f) EDS elemental mapping of the sample shown in (c).*

The morphology of WS_2/MoS_2 was scanned by HR-TEM. According to the TEM image (**Figure 8a**), WS_2/MoS_2 maintains a characteristic lamellar structure. The EDS elemental mapping of the sample shown in Figure 8a evinces no segregation (**Figure S2**). From inside to outside, the SAED elongated spots could correspond to (100)/(101), (103), and (110) planes of WS_2 as well as MoS_2, respectively, due to their isostructural nature (similar crystal system and lattice constants) (see **Figure 8b**). Therefore, this SAED image could derive from superimposing the aforementioned patterns.[48] Furthermore, the detection of these elongated spots confirms the existence of polycrystalline material. In the selected HR-TEM image (**Figure 8c**), W-containing nanodomains with high crystallinity are visualized. The observed interplanar d-spacings of ≈0.27, 0.32, and 0.60 nm are attributable to (100)/(101), (004), and (002) planes of WS_2, respectively.[35,49] In light of the good matching between W and Mo signals shown in the EDS elemental mapping (**Figures 8d, 8e** and **8f**), it can be concluded that W-containing nanopatches are homogeneously distributed over MoS_2 flakes.

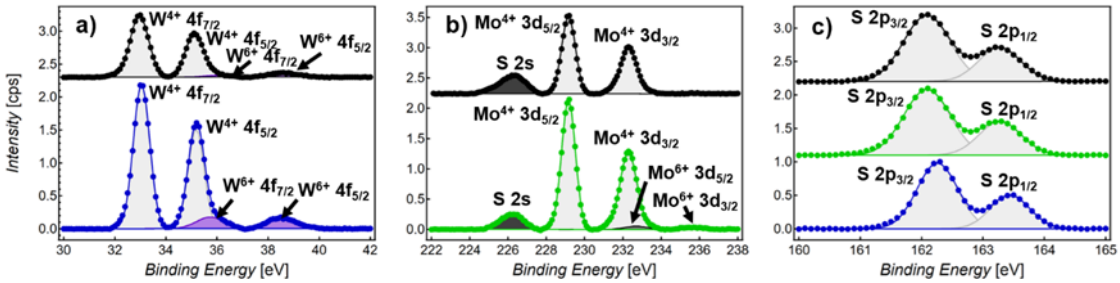

Figure 9. *a) W 4f XPS spectra of commercial WS_2 (blue) and WS_2/MoS_2 (black) normalized using the S $2p_{3/2}$ signal; b) Mo 3d XPS spectra of commercial MoS_2 (bright green) and WS_2/MoS_2 (black) using the S $2p_{3/2}$ signal; c) Normalized S 2p XPS spectra of commercial WS_2 (blue), commercial MoS_2 (bright green) and WS_2/MoS_2 (black).*

The chemical composition of WS_2/MoS_2 was investigated by XPS. W 4f spectrum (**Figure 9a**) perfectly resembles that of the material obtained after calcination of the W_3S_4 cluster as well as that of the commercial 2H-WS_2. Mo 3d spectrum (**Figure 9b**) shows three peaks located at ≈226.2, 229.2 and 232.3 eV, which correspond to S^{2-} 2s, Mo^{4+} $3d_{5/2}$ and Mo^{4+} $3d_{3/2}$ components in the thermodynamically stable 2H-MoS_2 phase, respectively.[42] As expected, Mo 3d spectrum perfectly resembles that of commercial 2H-MoS_2. S 2p spectrum (**Figure 9c**) displays two well-defined peaks at ≈162.1 and 163.3 eV, which are assigned to S^{2-} $2p_{3/2}$ and $2p_{1/2}$ components from both 2H-MoS_2 and 2H-WS_2, respectively. Whilst Mo:W molar ratio was estimated at 1.42, S:(Mo+W) molar ratio from MS_2 species was determined as 2.28. Apparently, the latter value deviates from the stoichiometry expected for WS_2 as well as MoS_2. However, for bulk WS_2 and MoS_2, S:W and S:Mo molar ratios (≈2.33 and 2.32, respectively) are comparable to the previous one. Even though that ce-MoS_2 flakes were mixed with $[W_3S_4(tu)_8(H_2O)]Cl_4{\cdot}2H_2O$ in a molar proportion of 1:5, respectively, the loss of W could be explained according to *i*) the removal of unattached W_3S_4 cluster *via* sequential washing redispersion/centrifugation cycles, and *ii*) the generation of volatile tungsten oxide hydrates (*e.g.*, $WO_2(OH)_2$)[47] and halides (*e.g.*, WCl_6).

In order to gain a better insight into the nature and thickness of the material formed over MoS_2 flakes, WS_2@MoS_2 was also inspected by Raman spectroscopy at 532 nm excitation wavelength. Consistently, the spectrum (**Figure 7b**) only reveals peaks related to both 2H-WS_2 and 2H-MoS_2.[50] Whilst peaks appearing at ≈353, and 416 cm^{-1} correspond to 2H-WS_2,[38] the rest of them (located at ≈382 and 406 cm^{-1}) are ascribable to 2H-MoS_2.[51] The absence of J peaks indicates a total 1T→2H polytype transformation. The coexistence of two clearly distinguishable pairs of E^1_{2g}/A_{1g} peaks, one per chalcogenide, discards the presence of alloyed $Mo_xW_{1-x}S_2$ materials.[48,52–54] In addition, the peak separation between $2LA/E^1_{2g}$ and A_{1g} modes (≈63 cm^{-1}) for WS_2 is also

consistent with few-layered nanosheets (presumably, mono- and bilayers).[40] The long-range Raman spectrum of WS_2@MoS_2 can be seen in the Supporting Information (**Figure S3**).

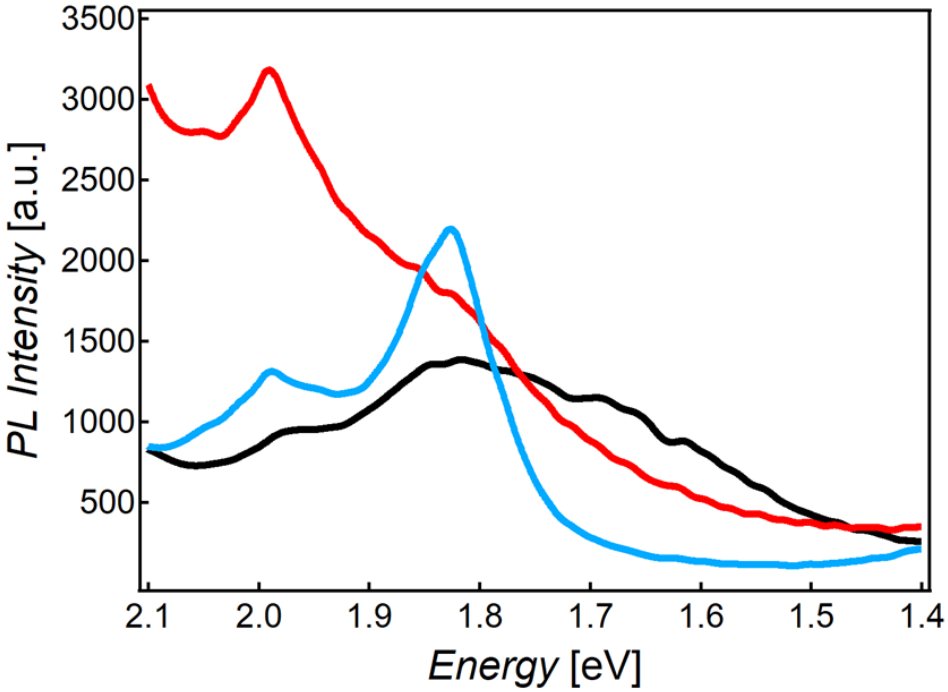

Figure 10. *PL spectra of WS_2 layers obtained through W_3S_4 cluster decomposition (red), ce-MoS_2 flakes treated under the same conditions used for preparing WS_2/MoS_2 heterostructure (blue), and WS_2/MoS_2 heterostructure (black).*

Finally, photoluminescence (PL) measurements were carried out to get some information about the strength of the interaction between WS_2 and MoS_2 in the heterostructure (**Figure 10**). As expected, the spectrum of thermally treated ce-MoS_2 flakes presents two peaks at 1.80 eV and 1.97 eV, characteristic of A1 and B1 excitonic transitions in ultrathin MoS_2 layers, while the spectrum of WS_2 layers shows the excitonic transition at 1.97 eV. In the case of WS_2/MoS_2 heterostructure, no clear peaks are detected in the corresponding spectrum. Interestingly, the intensity of this spectrum exhibits a dramatic decrease if compared to thermally threated ce-MoS_2 flakes. Indeed, it is well-known that the band alignment of WS_2 and MoS_2 layers in heterostructures prevents from the formation of correlated electron-hole pairs. Succinctly, the photogenerated holes are accumulated into WS_2 valence band while photogenerated electrons are promoted to MoS_2 conduction band.[18,55] As a result, the quenching of the PL signal observed for the present WS_2/MoS_2 heterostructure, can be considered as an evidence of the interaction between both dichalcogenides, which can exchange charge and energy, proving potential optoelectronic applications in the fields of light harvesting or photocatalysis.

Conclusion

In summary, in this paper we have reported a straightforward two-step strategy for preparing WS_2/MoS_2 heterostructures. In the first step, a homogeneous functionalization of MoS_2 surface is achieved thanks to the electrostatic interactions existing between negatively charged ce-MoS_2 flakes and $[W_3S_4(tu)_8(H_2O)]^{4+}$ cations dissolved in methanol. In the second step, the previous composite is calcined to give rise to heterostructures made from few-layer MoS_2 coated with mono- and/or bi-layer WS_2 coming from the thermal decomposition of the W_3S_4 cluster. The presence of specific electrostatic forces between ce-MoS_2 and W_3S_4 cluster can avoid the agglomeration of the cluster and ensure a better coverage of the ce-MoS_2 underlying flakes. This results in a homogeneous distribution of thin WS_2 flakes all over MoS_2 surface. Besides, the dry thermal treatment involved in the synthetic strategy guaranties the removal of all residues that could hinder a strong interaction between both TMDCs, which seems to be actually supported by the experimental PL measurements. Therefore, the combination of a simple, scalable and low-cost solution approach with a dry thermal decomposition, not only offers the advantages of most commonly used methods in solution, but also allows the good matching between 2D counterparts in the heterostructure usually reached by more complex physical strategies like CVD, PVD or deterministic transfer followed by annealing treatment. Interestingly, the proposed strategy could be applied to the synthesis of other 2D/2D heterostructures formed by thermally generated WS_2 or MoS_2 flakes on different anionic layers.

Experimental Section

Materials: Molybdenum(IV) sulphide and *n*-butyllithium solution 1.6 M in hexane were acquired from Alfa Aesar and Sigma-Aldrich, respectively. Milli-Q water was employed in all the experiments. Solvents were used without further purification. W_3S_4 cluster was prepared according to the protocol developed by A. L. Gushchin et al.[32]

Synthesis of WS_2 layers: $[W_3S_4(tu)_8(H_2O)]Cl_4{\cdot}2H_2O$ was calcined in the 25–700 °C range under a 10 °C min^{-1} scan rate and N_2 flow of 100 mL min^{-1}. The resultant material was preserved from the air exposure inside the TGA apparatus until it was cooled down to room temperature.

Synthesis of cluster@MoS_2: The volume corresponding to ≈13.5 μmol of ce-MoS_2 flakes was poured into 4 mL of $[W_3S_4(tu)_8(H_2O)]Cl_4{\cdot}2H_2O$ (100.0 mg, ≈67.4 μmol) in MeOH. Subsequently, the mixture was magnetically stirred for 1 h under argon at room temperature. Then, it was centrifuged at 13.4 krpm for 1.5 h. After decanting the supernatant, the sediment was dispersed in methanol and centrifuged at 13.4 krpm for 0.5 h. The previous dispersion-centrifugation-collection step was repeated once more. Finally, the sediment was dried by vacuum for at least 7 h.

Synthesis of WS_2/MoS_2: The previous composite was calcined in the 25–700 °C range under a 10 °C min^{-1} scan rate and N_2 flow of 100 mL min^{-1}. The resultant material was preserved from the air exposure inside the TGA apparatus until it was cooled down to room temperature.

Thermogravimetric Analysis (TGA): Thermogravimetric analysis was conducted at the Universidad de Alicante (Unidad de Análisis Térmico y Sólidos Porosos) with a Mettler Toledo TGA/SDTA851/1100/SF apparatus in the 25–700 °C range under a 10 °C min^{-1} scan rate and N_2 flow of 100 mL min^{-1}.

Transmission electron microscopy (TEM) and dark field scanning transmission electron microscopy (STEM): Samples were prepared by dropping methanolic suspensions on lacey

formvar/carbon copper grids (300 mesh). HR-TEM studies were carried out on a Technai G2 F20 microscope as well as a JEOL 2100 FEG-TEM microscope, both of them operating at 200 kV.

Raman and photoluminescence (PL) spectroscopy: Raman and PL spectra were recorded with a Raman Emission Horiba-MTB Xplora Spectrometer in ambient condition onto a substrate (532 nm). A 100x objective was used to focus the laser beam. For Raman measurements, powder samples were measured onto a clean SiO_2 (285 nm)/Si substrate. For PL measurements, with the aim of minimizing restacking effects, dispersions of calcined materials (5 min. sonication in degassed methanol) were spin-coated onto clean SiO_2 (285 nm)/Si substrates.

X-Ray Photoelectron Spectroscopy: Samples were analysed ex situ at the X-ray Spectroscopy Service at the Universidad de Alicante using a K-ALPHA Thermo Scientific spectrometer. All spectra were collected using Al Kα radiation (1486.6 eV), monochromatized by a twin crystal monochromator, yielding a focused X-ray spot (elliptical in shape with a major axis length of 400 μm) at 30 mA and 2 kV. The alpha hemispherical analyser was operated in the constant energy mode with survey scan pass energies of 200 eV to measure the whole energy band and 50 eV in a narrow scan to selectively measure the particular elements. XPS data were analysed with Avantage software. A smart background function was used to approximate the experimental backgrounds. Charge compensation was achieved with the system flood gun that provides low energy electrons and low energy argon ions from a single source. To determine molar ratios in WS_2 (from W_3S_4 cluster calcination), cluster@MoS_2 and WS_2/MoS_2, oxide contributions were ignored.

Acknowledgements

The authors acknowledge the financial support from the Spanish MINECO (Grants MAT2017-89528 and CTQ2017-89993, and Excellence Unit María de Maeztu MDM-2015-0538), the European Union (ERC-Advanced Grant MOL-2D and COST-MOLSPIN-CA15128 Molecular Spintronics Project) and the Generalitat Valenciana (Prometeo Program of Excellence and GentT program: CIDEGENT/2018/005). M.M.-G. and I.B. thank the Spanish MINECO for the F.P.U. fellowships. S.T. thanks the Spanish MINECO for a Ramón y Cajal Contract (RYC-2016-19817). A.F.-A. thanks the Universitat de València for a Senior Researcher contract. Moreover, authors are very grateful to Dr. Garin Escorcia-Ariza for their suggestions concerning the design of the figures and to Dr. Raúl Arenal from the Instituto Universitario de Investigación de Nanociencia de Aragón (Universidad de Zaragoza) for his helpful discussion about TEM images.

1 K. S. Novoselov, A. Mishchenko, A. Carvalho and A. H. Castro Neto, *Science*, **2016**, *353*, 6298.

2 P. T. K. Loan, W. Zhang, C.-T. Lin, K.-H. Wei, L.-J. Li and C.-H. Chen, *Adv. Mater.*, **2014**, *26*, 4838–4844.

3 Y. Liu, N. O. Weiss, X. Duan, H. C. Cheng, Y. Huang and X. Duan, *Nat. Rev. Mater.*, **2016**, *1*, 16042.

4 Y. Wang, Q. Wang, X. Zhan, F. Wang, M. Safdar and J. He, *Nanoscale*, **2013**, *5*, 8326–8339.

5 Q. H. Wang, K. Kalantar-Zadeh, A. Kis, J. N. Coleman and M. S. Strano, *Nat. Nanotechnol.*, **2012**, *7*, 699–712.

6 E. Navarro-Moratalla, J. O. Island, S. Mañas-Valero, E. Pinilla-Cienfuegos, A. Castellanos-Gomez, J. Quereda, G. Rubio-Bollinger, L. Chirolli, J. A. Silva-Guillén, N. Agraït, G. A. Steele, F. Guinea, H. S. J. Van Der Zant and E. Coronado, *Nat. Commun.*, **2016**, *7*, 11043.

7 J. A. Wilson and A. D. Yoffe, *Adv. Phys.*, **1969**, *18*, 193–335.

8 S. Ippolito, A. Ciesielski and P. Samorì, *Chem. Commun.*, **2019**, *55*, 8900–8914.

9 K. S. Novoselov, D. Jiang, F. Schedin, T. J. Booth, V. V. Khotkevich, S. V. Morozov and A. K. Geim, *Proc. Natl. Acad. Sci. U. S. A.*, **2005**, *102*, 10451–10453.

10 M. Chhowalla, H. Shin, G. Eda and L. Li, *Nat. Chem.*, **2013**, *5*, 263–275.

11 J. Xu, J. Zhang, W. Zhang and C.-S. Lee, *Adv. Energy Mater.*, **2017**, *7*, 1700571.

12 T. Y. Chen, Y. H. Chang, C. L. Hsu, K. H. Wei, C. Y. Chiang and L. J. Li, *Int. J. Hydrogen Energy*, **2013**, *38*, 12302–12309.

13 A. Pospischil, M. M. Furchi and T. Mueller, *Nat. Nanotechnol.*, **2014**, *9*, 257–261.

14 M. M. Furchi, A. Pospischil, F. Libisch, J. Burgdörfer and T. Mueller, *Nano Lett.*, **2014**, *14*, 4785–4791.

15 D. Merki and X. Hu, *Energy Environ. Sci.*, **2011**, *4*, 3878–3888.

16 J. Kang, S. Tongay, J. Zhou, J. Li and J. Wu, *Appl. Phys. Lett.*, **2013**, *102*, 01211

17 A. K. Singh, K. Mathew, H. L. Zhuang and R. G. Hennig, *J. Phys. Chem. Lett.*, **2015**, *6*, 1087–1098.

18 X. Hong, J. Kim, S. F. Shi, Y. Zhang, C. Jin, Y. Sun, S. Tongay, J. Wu, Y. Zhang and F. Wang, *Nat. Nanotechnol.*, **2014**, *9*, 682–686.

19 K. Chen, X. Wan, W. Xie, J. Wen, Z. Kang, X. Zeng, H. Chen and J. Xu, *Adv. Mater.*, **2015**, *27*, 6431–6437.

20 P. C. Sherrell, P. Palczynski, M. S. Sokolikova, F. Reale, F. M. Pesci, M. Och and C. Mattevi, *ACS Appl. Energy Mater.*, **2019**, *2*, 5877–5882.

21 F. M. Pesci, M. S. Sokolikova, C. Grotta, P. C. Sherrell, F. Reale, K. Sharda, N. Ni, P. Palczynski and C. Mattevi, *ACS Catal.*, **2017**, *7*, 4990–4998.

22 C. Lu, J. Ma, K. Si, X. Xu, C. Quan, C. He and X. Xu, *Phys. status solidi*, **2019**, 1900544.

23 B. V. Lotsch, *Annu. Rev. Mater. Res.*, **2015**, *45*, 85–109.

24 T. Sasaki, Y. Ebina, T. Tanaka, M. Harada, M. Watanabe and G. Decher, *Chem. Mater.*, **2001**, *13*, 4661–4667.

25 E. Coronado, C. Martí-Gastaldo, E. Navarro-Moratalla, A. Ribera, S. J. Blundell and P. J. Baker, *Nat. Chem.*, **2010**, *2*, 1031–1036.

26 M. Q. Yang, Y. J. Xu, W. Lu, K. Zeng, H. Zhu, Q. H. Xu and G. W. Ho, *Nat. Commun.*, **2017**, *8*, 14224

27 B. W. Li, M. Osada, T. C. Ozawa, Y. Ebina, K. Akatsuka, R. Ma, H. Funakubo and T. Sasaki, *ACS Nano*, **2010**, *4*, 6673–6680.

28 S. Luo, S. Dong, C. Lu, C. Yu, Y. Ou, L. Luo, J. Sun and J. Sun, *J. Colloid Interface Sci.*, **2018**, *513*, 389–399.

29 H. Zhou, F. Yu, J. Sun, R. He, Y. Wang, C. F. Guo, F. Wang, Y. Lan, Z. Ren and S. Chen, *J. Mater. Chem. A*, **2016**, *4*, 9472–9476.

30 J. Luxa, J. Fawdon, Z. Sofer, V. Mazánek and M. Pumera, *ChemPhysChem*, **2016**, *17*, 2890–2896.

31 M. Morant-Giner, R. Sanchis-Gual, J. Romero, A. Alberola, L. García-Cruz, S. Agouram, M. Galbiati, N. M. Padial, J. C. Waerenborgh, C. Martí-Gastaldo, S. Tatay, A. Forment-Aliaga and E. Coronado, *Adv. Funct. Mater.*, **2018**, *28*, 1706125.

32 Y. A. Laricheva, A. L. Gushchin, P. A. Abramov and M. N. Sokolov, *J. Struct. Chem.*, **2016**, *57*, 962–969.

33 A. L. Gushchin, Y. A. Laricheva, P. A. Abramov, A. V. Virovets, C. Vicent, M. N. Sokolov and R. Llusar, *Eur. J. Inorg. Chem.*, **2014**, *2014*, 4093–4100.

34 A. L. Gushchin, Y. A. Laricheva, M. N. Sokolov, and R. Llusar, *Russ. Chem. Rev.*, **2018**, *87*, 670–706.

35 W. J. Schutte, J. L. De Boer and F. Jellinek, *J. Solid State Chem.*, **1987**, *70*, 207–209.

36 B. Mahler, V. Hoepfner, K. Liao and G. A. Ozin, *J. Am. Chem. Soc.*, **2014**, *136*, 14121–14127.

37 J. C. Kotsakidis, Q. Zhang, A. L. Vazquez de Parga, M. Currie, K. Helmerson, D. K. Gaskill and M. S. Fuhrer, *Nano Lett.*, **2019**, *19*, 5205–5215.

38 A. Berkdemir, H. R. Gutiérrez, A. R. Botello-Méndez, N. Perea-López, A. L. Elías, C. I. Chia, B. Wang, V. H. Crespi, F. López-Urías, J. C. Charlier, H. Terrones and M. Terrones, *Sci. Rep.*, **2013**, *3*, 1755.

39 F. Wang, I. A. Kinloch, D. Wolverson, R. Tenne, A. Zak, E. O'Connell, U. Bangert and R. J. Young, *2D Mater.*, **2016**, *4*, 015007.

40 A. A. Mitioglu, P. Plochocka, G. Deligeorgis, S. Anghel, L. Kulyuk and D. K. Maude, *Phys. Rev. B - Condens. Matter Mater. Phys.*, **2014**, *89*, 245442.

41 K. C. Knirsch, N. C. Berner, H. C. Nerl, C. S. Cucinotta, Z. Gholamvand, N. McEvoy, Z. Wang, I. Abramovic, P. Vecera, M. Halik, S. Sanvito, G. S. Duesberg, V. Nicolosi, F. Hauke, A. Hirsch, J. N. Coleman and C. Backes, *ACS Nano*, **2015**, 9, 6018–30.

42 X. Geng, W. Sun, W. Wu, B. Chen, A. Al-Hilo, M. Benamara, H. Zhu, F. Watanabe, J. Cui and T. P. Chen, *Nat. Commun.*, **2016**, *7*, 10672.

43 M. A. Lukowski, A. S. Daniel, F. Meng, A. Forticaux, L. Li and S. Jin, *J. Am. Chem. Soc.*, **2013**, *135*, 10274–10277.

44 X. Fan, P. Xu, D. Zhou, Y. Sun, Y. C. Li, M. A. T. Nguyen, M. Terrones and T. E. Mallouk, *Nano Lett.*, **2015**, *15*, 5956–5960.

45 A. P. Nayak, T. Pandey, D. Voiry, J. Liu, S. T. Moran, A. Sharma, C. Tan, C.-H. Chen, L.-J. Li, M. Chhowalla, J.-F. Lin, A. K. Singh and D. Akinwande, *Nano Lett.*, **2015**, *15*, 346–53.

46 L. M. Vogl, P. Schweizer, M. Wu and E. Spiecker, *Nanoscale*, **2019**, *11*, 11687–11695.

47 Y. Ma, J. Li, W. Liu and Y. Shi, *Nanoscale Res. Lett.*, **2012**, *7*, 325.

48 J. M. Woods, Y. Jung, Y. Xie, W. Liu, Y. Liu, H. Wang and J. J. Cha, *ACS Nano*, **2016**, *10*, 2004–2009.

49 R. G. Dickinson and L. Pauling, *J. Am. Chem. Soc.*, **1923**, *45*, 1466–1471.

50 L. Li, R. Ma, Y. Ebina, N. Iyi and T. Sasaki, *Chem. Mater.*, **2005**, *17*, 4386–4391.

51 H. Li, Q. Zhang, C. C. R. Yap, B. K. Tay, T. H. T. Edwin, A. Olivier and D. Baillargeat, *Adv. Funct. Mater.*, **2012**, 22, 1385–1390.

52 J. G. Song, G. H. Ryu, S. J. Lee, S. Sim, C. W. Lee, T. Choi, H. Jung, Y. Kim, Z. Lee, J. M. Myoung, C. Dussarrat, C. Lansalot-Matras, J. Park, H. Choi and H. Kim, *Nat. Commun.*, **2015**, *6*, 7817

53 Z. Wang, P. Liu, Y. Ito, S. Ning, Y. Tan, T. Fujita, A. Hirata and M. Chen, *Sci. Rep.*, **2016**, 6, 21536.

54 X. Liu, J. Wu, W. Yu, L. Chen, Z. Huang, H. Jiang, J. He, Q. Liu, Y. Lu, D. Zhu, W. Liu, P. Cao, S. Han, X. Xiong, W. Xu, J.-P. Ao, K.-W. Ang and Z. He, *Adv. Funct. Mater.*, **2017**, 27, 1606469.

55 L. P. L. Mawlong, A. Bora and P. K. Giri, *Sci. Rep.*, **2019**, *9*, 19414.

Supporting Information

WS_2/MoS_2 heterostructures via thermal treatment of MoS_2 layers electrostatically functionalized with W_3S_4 molecular clusters

Marc Morant-Giner, Isaac Brotons, Nikita Y. Shmelev, Artem L. Gushchin, Luke Norman, Andrei N. Khlobystov, Antonio Alberola, Sergio Tatay, J. Canet-Ferrer, Alicia Forment-Aliaga* and Eugenio Coronado*

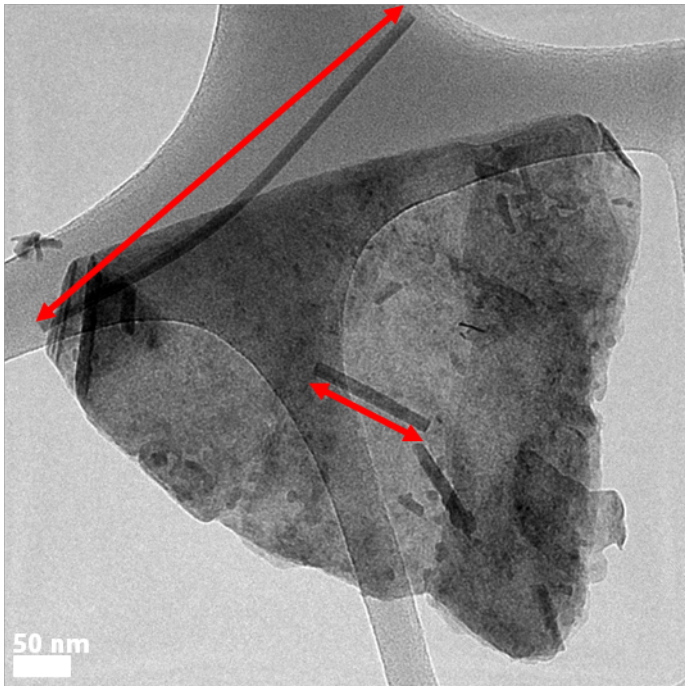

Figure S1. *TEM image of WS_2@MoS_2 showing MoO_2 nanowires.*

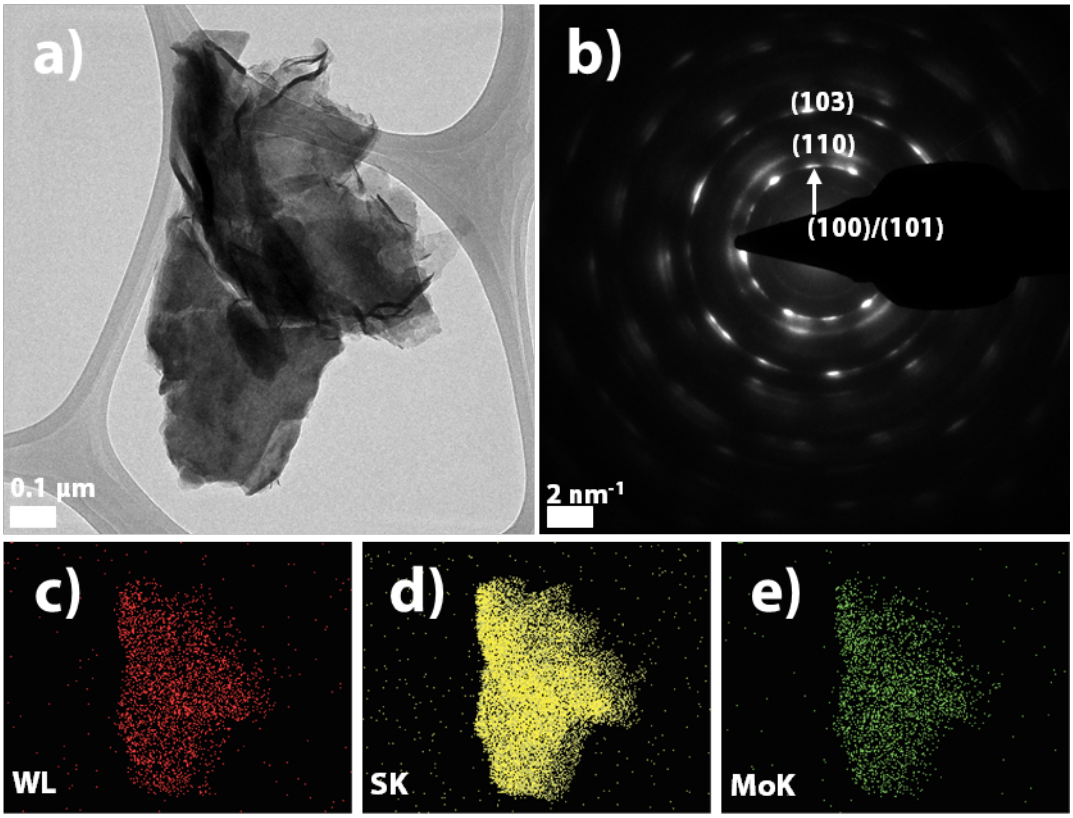

Figure S2. *a) TEM image of WS_2@MoS_2, b) SAED pattern of the sample shown in (a); c-e) EDS elemental mapping of the sample shown in (a).*

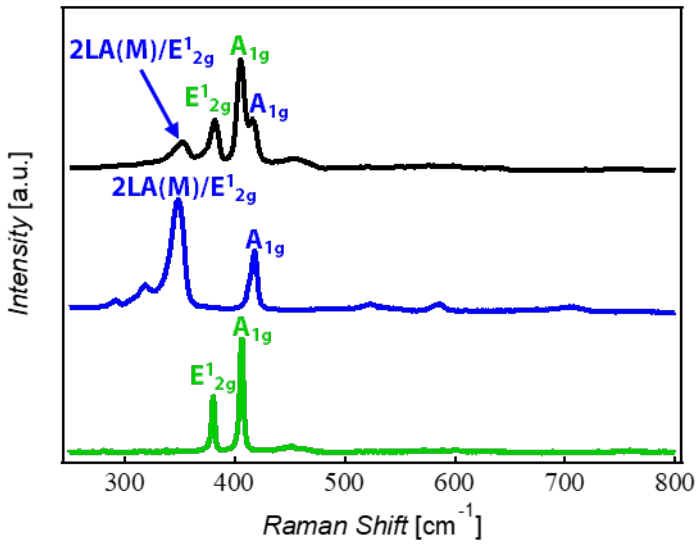

Figure S3. *Long-range Raman spectra of commercial MoS_2 (bright green), commercial WS_2 (blue) and WS_2@MoS_2 (black).*